This is a repository copy of *Electrochemical response of micro-alloyed steel under potentiostatic polarization in CO₂ saturated brine*.

White Rose Research Online URL for this paper:
http://eprints.whiterose.ac.uk/129437/

Version: Accepted Version

Article:

ELECTROCHEMICAL RESPONSE OF MICRO-ALLOYED STEEL UNDER POTENTIOSTATIC POLARIZATION IN CO₂ SATURATED BRINE

[1]Lawrence Onyeji, [2]Sikiru Mohammed, [1]Girish Kale*.
[1]School of Chemical and Process Engineering, University of Leeds, Leeds, LS2 9JT, United Kingdom.

[2]Institute of Functional Surfaces, Department of Mechanical Engineering, University of Leeds, United Kingdom.

pmlio@leeds.ac.uk; (+447466099454).
*G.M.Kale@leeds.ac.uk; (+44(0)1133432805, +44(0)7946476869) Corresponding Author
mnsam@leeds.ac.uk;

Abstract

Corrosion scales were formed on micro-alloyed steel designated as P110X and compared with API 5L X65 in CO_2 saturated 3.5wt% NaCl at 60^0C and pH 6.5 using Potentiostatic polarization at three different anodic potentials for 24 hours. The electrochemical behaviour of the corrosion scales were investigated using EIS and surface analysis techniques. The results revealed that the scales were non-protective demonstrating a decrease in film stability with increase in potential. It was generally observed that due to chemical composition and microstructures API 5L X65 exhibited better general corrosion resistance but showed more prone to pitting corrosion than steel P110X.

Keywords: A - Steel,   B - Potentiostatic,   B - EIS,   B - SEM,   C - Acid corrosion.

1.0 Introduction

Micro-alloying of steels was first reported in early 1920s by A. L. Field and F. M. Becket when Zr was added to plain carbon steel. However, the term micro-alloying was scientifically recognised from 1959 with the addition of Nb to carbon steels[1]. From this period, micro-alloyed (high-strength low-alloy - HSLA) steels have become an important class of structural materials [2] providing desirable combinations of excellent properties which could not be attained with conventional carbon steel [3]. Micro-alloyed steels cost less than carbon steel and low alloy steel and have been materials of choice in auto mobile and oil and natural gas industries[4]. This excellent combination of properties can be attributed to the presence of fine grain structures achieved by the addition of small quantity of alloying elements, controlled processing technologies and appropriate heat treatments[3, 5]. The extensive use of micro-alloyed steels is based on a number of factors such as (1) the ability to form protective corrosion film that covers the surface of the steel (thereby physically blocking the corrosion species from reaching the substrate and thus reduced corrosion rate), (2) the use of corrosion inhibitors, (3) availability of iron and (4) relatively low production cost [6-8].

Both experimental and field evidence have shown that sweet (CO_2) corrosion is the most challenging problem in the oil and gas industry leading to more than 60% failures in equipment and facility with the attendant capital expenditure (CAPEX) and operating expenditure (OPEX) [9, 10]. Dry CO_2 is by itself non-corrosive but hydrates in the presence of water to carbonic acid (H_2CO_3), a weak but corrosive acid. Carbonic acid (H_2CO_3) dissociates in two steps to bicarbonate (HCO_3^-) and carbonate (CO_3^{2-}) ions respectively. These ions, depending on temperature, pH and CO_2 partial pressure react with oxidized ferrous (Fe^{2+}) ion to form iron carbonate ($FeCO_3$). This involves a sequence of chemical and electrochemical reactions as summarised by Hany, et al [6]:

The precipitation of $FeCO_3$ is thermodynamically possible as in Eq. 1 when the concentrations of ferrous ions ($C_{Fe^{2+}}$) and carbonic ions ($C_{CO_3^{2-}}$) exceed the solubility product (K_{sp}) of $FeCO_3$[11, 12]. The driving force for precipitation of $FeCO_3$ is the super-saturation level which is defined in Eq. 7

$$S_{FeCO_3} = \frac{C_{Fe^{2+}} {}_* C_{CO_3^{2-}}}{K_{sp}} \tag{7}$$

Where C is concentration and K_{sp} is the solubility product of $FeCO_3$.

Stainless steels when exposed to an oxidizing environment spontaneously form extremely thin passive films of Cr_2O_3 on the surface. These passive films offer significant protection leading to increase in corrosion resistance. The effect of passive films on the corrosion resistance of stainless steel have been extensively reported in literature. Luo, et al[13] potentiostatically grew passive film on stainless steels at different potential values chosen within the passive and trans-passive regions in 1 wt% NaCl. The EIS results demonstrated that the corrosion behaviour of the steels was significantly affected by the potential used in forming the passive films. It shows that increasing the formation potential within the passive section, increased the corrosion resistance but showed opposite behaviour within the trans-passive section. Della, et al [14, 15] observed similar corrosion behaviour within the passive and trans-passive regions of shape memory stainless steels (SMSSs) in acidic environment and they reported that the structure, thickness, composition, and semiconducting properties of the film determine the protectiveness of passive films formed on stainless steels.

Depending on the environmental conditions in the bulk solution, actively corroding steels in carbon dioxide saturated solution may form protective or non-protective corrosion products [9, 16]. $FeCO_3$ is the main corrosion product of carbon steel in CO2 environment. The protectiveness of $FeCO_3$ depends on the materials characteristics and environmental parameters [17]. The effects of these parameters on the formation mechanism of $FeCO_3$ and its subsequent protective properties have been widely studied [8, 18, 19].

Alizadeh and Boardbar [18] investigated the protectiveness of corrosion scale formed on weld joints of steel grade API X70 after 90 days immersion in a mixture of three sodium salts at different concentrations and pH 9.7. The results showed that microstructures occasioned by heat treatment have significant effects on the electrochemical behaviour of the steel. Using potentiostatic polarization, Sun, et al [9] grew corrosion product scales on low alloyed steels at different time and employed EIS to investigate the electrochemical characteristics of the corrosion scale. The results showed that the electrochemical behaviour is associated with the formation of corrosion product scale which in turn depend on the microstructure of the steel. Islam and Farhat [20] formed corrosion product layer on API X42 by immersion in CO_2 saturated 2 g/l NaCl solution at different time schedule and characterized the corrosion scale using SEM, XRD and XPS. Very few studies have been conducted on the stability and protectiveness of potentiostatically grown corrosion product on micro-alloyed steels in CO_2 saturated brine. In this work, corrosion product films were anodically grown on the surface of micro-alloyed steel designated as P110X and compared with API 5L X65 steel at different formation potentials. Electrochemical Impedance Spectroscope (EIS) was used to observe the corrosion behaviour of the films while surface analysis techniques such as SEM/EDS, XRD and white light profilemetry were used to characterise the structure, thickness, composition of the film and pitting tendency.

2.0.   Experimental Procedures

2.1.   Materials and Electrolytes

A micro-alloyed steel of API equivalent grade ISO11960/API 5CT P110 PSL1 and designated as P110X with chemical composition shown in Table 1 was used in this work. The steel has a rectangular surface area of 2.88 cm^2 with a quenched and tempered ferrite-pearlite microstructure. API 5L X65 steel with cylindrical surface area of 4.91 cm^2 also with ferrite-pearlite microstructure and chemical composition listed in Table 1 was used as reference specimen. The SEM surface morphology of the supplied specimens are displayed in Fig. 1. Copper wire was welded on the non-working area of the specimens to serve as an electrical contact point with the potentiostat and then imbedded in a non-conductive resin leaving the test area uncovered.

Table 1: Chemical composition of the test sample (wt%)

Steels	C	Si	Mn	P	S	Cr	V	Ti	Nb	Mo	Cu	Fe
P110X	0.22	0.032	1.4	0.012	0.001	0.25	0.005	0.023	0.002	0.07	0.03	Balance
X65	0.12	0.18	1.27	0.008	0.002	0.11	0.057	0.001	0.054	0.17	0.12	Balance

The test surface was sequentially grinded with silicon carbide paper to P1200 grit fineness. Acetone was used to erase any grease, while deionized water was employed to clean before the surface was dried

3

with warm air. The specimen was immediately immersed in a solution of 3.5 wt% NaCl in 1 litre glass cell at atmospheric pressure, 60^0C and pH 6.5 after CO_2 gas was bubbled for about 3 hours. The pH of the solution was adjusted using Hydrochloric acid (HCl) while the desired temperature was maintained using a hotplate with a controlled thermocouple immersed in the solution. The hotplate was set at a rotating speed of 200 rpm and with a magnetic stirrer, a homogeneous condition was maintained within the bulk electrolyte. Three tests were conducted for each specimen in order to ensure repeatability.
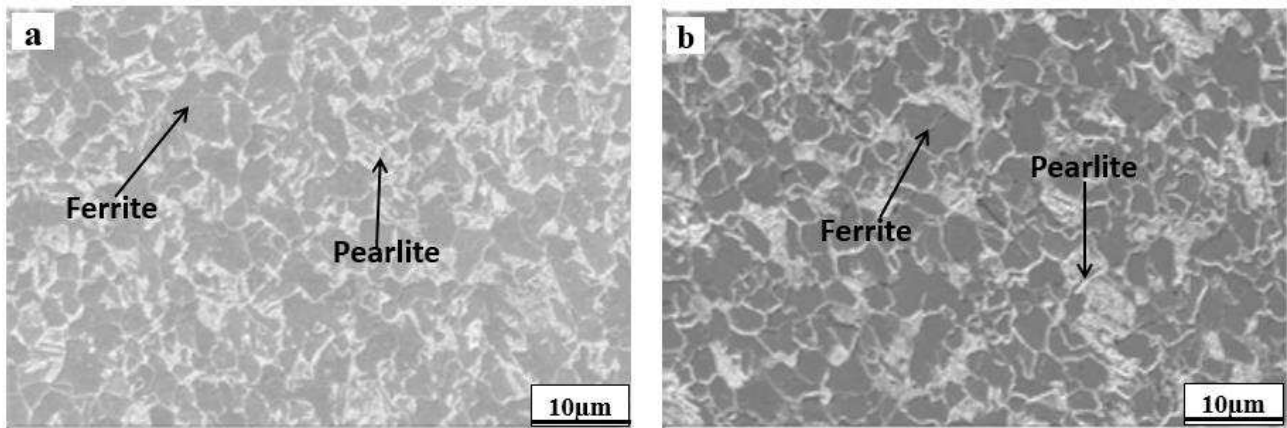

Fig. 1: SEM surface morphology of the supplied specimens (a) Steel P110X and (b) X65

2.2.   Potentiostaic polarization measurement

The conventional three-electrode electrochemical cell consisting of platinum counter electrode, Ag/AgCl reference electrode and the specimen as working electrode was used. Solartron analytical Model SI 1287 electrochemical interface analyser equipped with CorrWare and CorrView was used for potentiostatic polarization. Before the electrochemical measurements, the working electrodes were reduced potentiostatically at -800 mV vs open circuit potential (OCP) for 30 minutes to remove the surface oxide film formed while immersing the specimens into the electrolyte.   Corrosion Product films were then grown anodically on the specimens using applied potentials of 100, 150 and 200 mV vs OCP respectively for 24hours during which the evolution of current density were recorded versus time.

2.3.   Electrochemical impendence measurement

A two-electrode electrochemical cell, in which the steel specimen was the working electrode and platinum coil the counter electrode was used for electrochemical impedance spectroscopy (EIS). EIS measurement was conducted at OCP with potential perturbation of 5 mV and at a frequency range of 100 KHz to 0.1 Hz after 24 hours potentiostatic polarization. Solartron SI 1260 impedance/gain-phase analyser equipped with ZPlot was used for data collection while the experimental results were interpreted based on an equivalent electrical circuit by using a suitable fitting procedure of ZView.

2.4   Surface Analysis

After electrochemical tests, electrodes were removed, cleaned in deionized water and surface dried using warm air. The surface morphologies of the corrosion films were characterized using Carl Zeiss EVO MA15 with Oxford Instruments Aztec Energy EDS system while the phase analyses were obtained using XRD Bruker D8 Detector. Also the corroded steels were vertically embedded with epoxy resin, cross sectioned to reveal the thickness of the corrosion product, ground with silicon carbide paper to P1200 grit fineness and the properties of the exposed corrosion film characterized using SEM and Fiji ImageJ analysis.

The layers of the corrosion film on the surface of the specimens were chemically removed using a specific chemical solution consisting of 500mL of HCl, 450mL of deionized water and 5g of urotropine (hexamethylenetetramine). The specimens were vigorously stirred in the solution for 10 minutes, cleaned in deionized water and surface dried using warm air. The surface of the cleaned specimens was examined in SEM and pits were identified. The identified pits were characterized using white light interferometer. Top ten average pit depth were recorded for each test condition and repeated to obtain an average value. Pit identification was in accordance with standard procedures as stipulated in ASTM G46-94 for pitting corrosion examination and evaluation [21]. Multiple region analysis was used to obtain relevant statistics such as location and threshold of the formed pit depths. The scanned areas were stitched by adding a series of small datasets of suitable dimension.

3.0   Results and Discussions

3.1   Potentiostatic Polarization Measurements

Fig. 2 shows the evolution of current density versus time of the specimens for three anodically applied potentials in 3.5 wt% NaCl solution containing CO_2 at 60^0C and pH6.5. These plots show that the current density increased as the applied potential increased. This agreed with literature reports [7, 22, 23]which suggest that current density increased with potential within the active region due to activation control reaction. It is also evident from Fig. 2 that the measured current density of API 5L X65 steel is lower than that of steel P110X within the range of applied potential. This was ascribed to the variation in chemical composition and microstructures of the specimens. Steel P110X as shown in Table 1 has more carbon content with finer grain size. This translated to greater pearlite/ferrite ratio and more micro galvanic cells [24] which provided more surface area for corrosion attack [25].
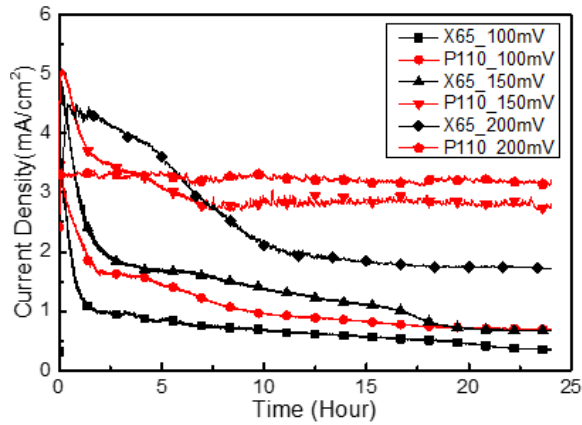
Fig 2: Evolution of current density with time of the specimens for 24 hours potentiostatic polarization at different anodic potentials in 3.5 wt% NaCl solution containing CO_2 at 60^0C and pH 6.5

3.2   Electrochemical Impedance Spectroscopy Measurements

Fig.3 shows the EIS spectra of P110X and X65 steels in CO_2 containing 3.5 wt% NaCl at 60^0C and pH 6.5 after corrosion product was grown at different anodic potentials for 24 hours. The specimens are actively corroding steels and the applied potentials were within the active regions. It can be seen from Fig.3 (a) that the Nyquist plots for the two steels in the three applied potentials displayed similar features of one semi-capacitive-Loops at high frequency resulting from the non-homogeneity of the surface, frequency dispersion and mass transport resistant[13, 25].
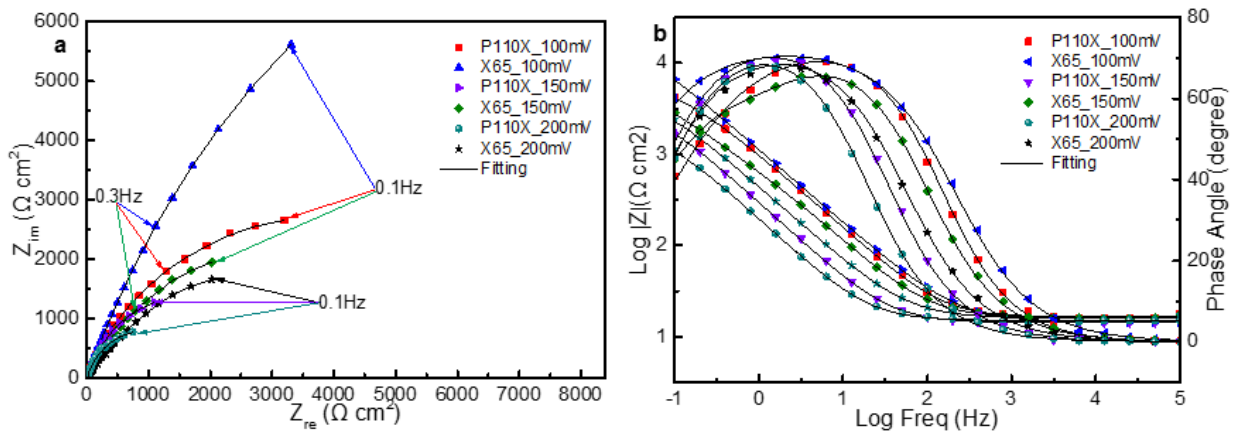

Fig 3: EIS plots of the specimens after potentiostatic polarization at different anodic potentials in 3.5 wt% NaCl solution containing CO_2 at 60^0C and pH 6.5. (A) Nyquist and (B) Bode

It can be seen from the Nyquist plots (Fig.3 (a)) that increase in applied anodic potential decreased the radius of the capacitive Loop demonstrating the effects of high applied potential on actively corroding steels. Experimental evidence have shown that increase in capacitive Loop indicates an increase in the film stability (ie ability to resist corrosion) and vice versa [26]. Thus it is obvious from Fig.3(a) that the impedance response for the film formed at 100mV$_{(OCP)}$ (particularly for X65) was higher when compared with that of 150 mV$_{(OCP)}$ and 200 mV$_{(OCP)}$ indicating better corrosion resistance for film formed at 100

6

$mV_{(OCP)}$. This shows that increasing the applied anodic potential decreases the radius of the semi-Loops. This is the characteristics of actively corroding steels that increase in potential increases the anodic current density [23]. This behaviour can be attributed to the ferrite-pearlite microstructure of the specimens as presented schematically by Sun, et al [9].

The radius of the impedance semi-Loop represents the interface resistance of the charge transfer which corresponds to the corrosion resistance[9, 25]. Similar work conducted using active-passive metals (alloy 59 in 0.5 m H_2SO_4 [27], ultrahigh-strength stainless steel in 1 wt% NaCl [13], shape memory stainless steels (SMSSs) in 0.5 M H_2SO_4 [15] and stainless steel type 304 in 0.5 M H_2SO_4 [15]) with different formation potentials within the passive region exhibited opposite results. These results indicated that for passive steels the capacitive Loops and the corresponding charge transfer resistance became larger as the applied potentials increased. This was attributed to the passive film which blocked the corrosive species from reaching the steel substrate. This means that the passive films formed at higher applied potentials are more protective and stable than that formed at lower applied potentials on active-passive steels. This is contrary to the behaviour observed with actively corroding micro-alloyed steels used in this work.

The Bode plots in Fig 3 (b) shows that the high frequency impedance magnitude ($|Z|$), which represents the solution resistance (R_s), is about 16 Ωcm^2 while the phase angle is 0^0 for both specimens and with all the applied potentials. This means that at high frequency, the impedance value is determined by the resistance of the electrolyte only. Alternatively, the charge transfer resistance (R_{ct}), which is the low frequency value of impedance lie between 3000 – 8000 Ωcm^2. The maximum phase angle values for all the specimens appeared within the intermediate frequencies with the specimen polarized at 100 mV $_{(OCP)}$ exhibiting the highest phase angle of 70^0. This shows that the phase angle values for the two steels decreased with increased anodic (applied) potentials. Similar trend was observed at the low frequency phase angles demonstrating medium values between 40^0 - 60^0 [13, 26]

To elucidate how applied anodic potentials affect the EIS results on the specimens in CO_2 containing 3.5 wt% NaCl solution at 60^0C and pH6.5, the simple Randle cell (equivalent circuit, EC) model consisting of a parallel combination of a double layer capacitance (C_{dl}) and a charge transfer resistance (R_{ct}) corresponding to the corrosion reactions at the metal/electrolyte interface and the electrolyte resistance (R_s) between the working and reference electrodes as shown in Fig. 4 was used. The constant phase element (CPE) was introduced in the equivalent circuit (EC) instead of pure double layer capacitance. This is to reduce the effect of surface irregularities and compositional inhomogeneity of the steels [13, 25]. The impedance of CPE is defined in Eq. 8.

$$Z_{CPE} = \frac{1}{Y_o} (j\omega)^{-n} \tag{8}$$

Where Y_o is the magnitude of CPE, $\omega = 2\pi f$ is the angular frequency, f is the ordinary frequency (measured in Hertz), j is the imaginary number and n is the dispersion coefficient related to surface non-homogeneity. Depending on the value of n, CPE may be pure resistor (ie if n = 0 then Z_0 = R), pure capacitor (meaning that n = 1 when Z_0 = C) or inductor (ie when n = 0.5 and Z_0 = W) [9, 25, 26].
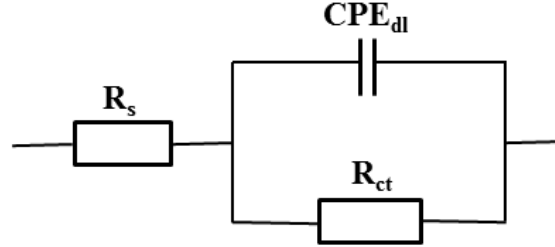

Fig 4: Equivalent circuit used for fitting EIS data of the specimen after 24 hours potentiostatic polarization at different anodic potentials in 3.5 wt% NaCl solution containing CO_2 at 60^0C and pH 6.5.

To validate the proposed EC, the simulated parameters and the % error of the impedance data obtained for the anodically polarised specimens are presented in Table 2. The virtually perfect fits of the Nyquist curves (Fig. 3(a)) and the simulated data attest to the reliability of the proposed equivalent circuit revealing acceptable relative % errors for the corresponding fitted values as indicated in Table 2. This table showed that as the applied potential increased, the CPE_{dl} representing the surface heterogeneity increased reflecting the porosity of the corrosion product film. Alternately, the charge transfer resistance, R_{ct}, decreased as the anodic potential increased indicating faster rate of reactions at the corrosion product/electrolyte interface. This signified that when the applied potential increased, the corrosion rate also increased. This effect was attributed to micro-galvanic effect. The EIS results are in agreement with the trend of the corrosion film formed at different potentials demonstrating a decline in impedance as the applied potential is increased [15, 23].

Table 2: Fitted EIS data for the specimens after 24 hours potentiostatic polarization at different potentials in 3.5 wt% NaCl solution containing CO_2 at 60^0C and pH6.5.

Potential (mV)	Specimens	Rs		CPE_{dl}		N		R_{ct}	
		Value ($\Omega.cm^2$)	% Error	Value ($\mu F^{-1} cm^{-2}$)	% Error	Value	% Error	Value ($K\Omega.cm^2$)	% Error
100	P110X	16.19	1.31	$2.2 * 10^{-4}$	2.38	0.983	0.68	6.514	5.48
	X65	14.39	1.6	$2.0 * 10^{-4}$	2.5	0.91	0.72	25.501	7.59
150	P110X	14.18	1.2	$6.70 * 10^{-4}$	2.4	0.87	0.92	3.526	8.75
	X65	15.78	1.4	$3.51 * 10^{-4}$	2.68	0.88	0.84	5.052	7.32
200	P110X	14,93	1.04	$7.04 * 10^{-4}$	2.25	0.82	0.84	1.993	7.08
	X65	15.4	1.18	$4.86 * 10^{-4}$	2.26	0.83	0.75	4.665	7.82

To further buttress the reliability and effectiveness of the fitted data for the proposed EC, the relative residual errors for the real (η_{re}) and imaginary (η_{im}) components of the impendence were calculated using Eqs. 9 and 10 respectively[23].

$$\eta_{re} = (\frac{Z_{re.exp} - Z_{re.fit}}{Z_{re.exp}}) * 100\% \qquad (9)$$

$$\eta_{im} = (\frac{Z_{im.exp} - Z_{im.fit}}{Z_{im.exp}}) * 100\% \qquad (10)$$

Where $Z_{re.exp}$ and $Z_{re.fit}$ are the real impedance obtained from EIS experimental results and EC fitting respectively while $Z_{im.exp}$ and $Z_{im.fit}$ are the imaginary impendences measured from EIS experimental results and EC fitting respectively. The residual errors can be used to elucidate the quality of the fitting obtained from the EC.

Fig. 5 shows the relative residual error curves from the equivalent circuits of the specimens after 24 hours potentiostaic polarization in 3.5 wt% NaCl solution containing CO_2 at 60^0C and pH 6.5. The two steels exhibited similar curves in all the applied potentials demonstrating relative error values within the range of 6% to 8%. This is almost the same with the values of the relative % errors obtained with ZView interpretation of the EC. This indicates that the quality of the fit is within acceptable error and attested to a good choice of EC.
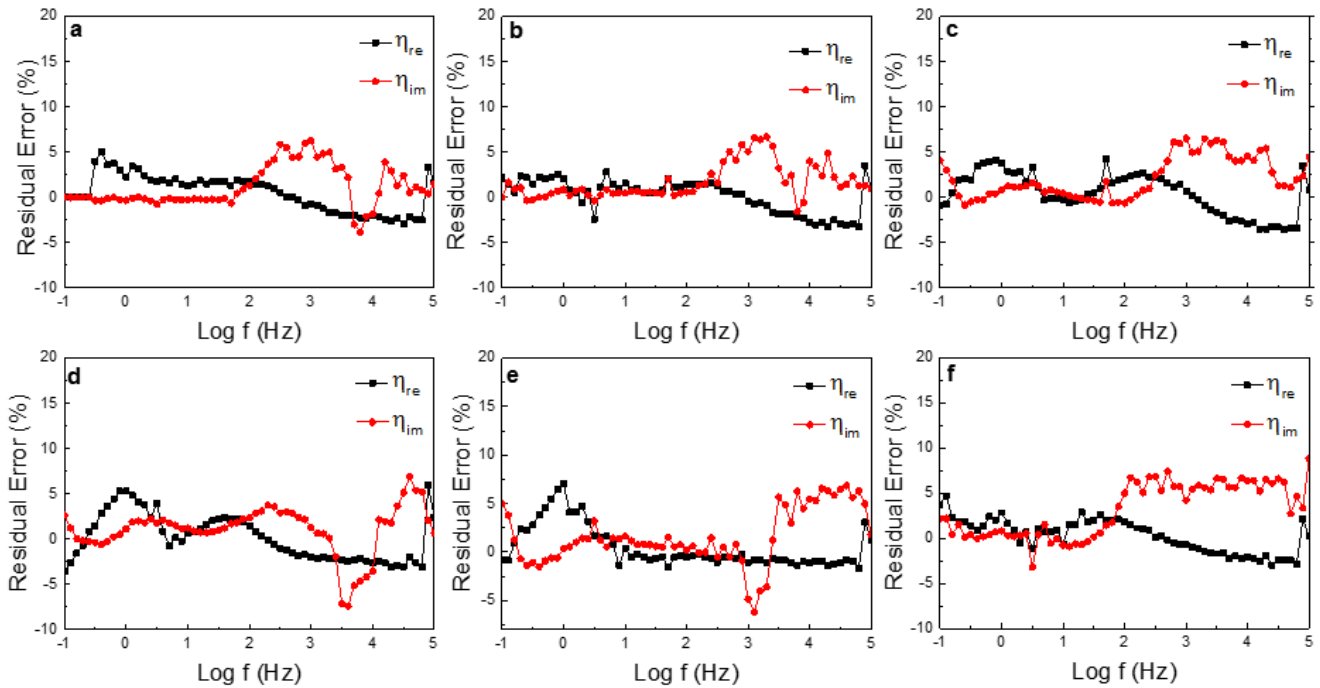
Fig 5: Relative residual error resulting from the equivalent circuits of the specimens after 24 h potentiostaic polarization in 3.5 wt% NaCl solution containing CO_2 at 60^0C and pH 6.5 for P110X (a) 100 mV$_{(OCP)}$, (b) 150 mV$_{(OCP)}$ and (c) 200mV$_{(OCP)}$; for X65 (d) 100 mV$_{(OCP)}$, (e) 150 mV$_{(OCP)}$ and (f) 200 mV$_{(OCP)}$

From the potentiostatic polarization and the impedance measurement results, it is observed that API 5L X65 steel demonstrated better resistance to general corrosion than steel P110X. This could be attributed to variation in microstructures and elemental specification of the steels [8]. Both steels consist of ferrite-pearlite microstructure as shown in Fig. 1. During an electrochemical corrosion of micro-alloyed steels consisting of ferrite-pearlite microstructures, the ferrite phase is selectively dissolved first while the pearlite (Fe + Fe$_3$C) phase is left on the surface of the steel undissolved. With further dissolution of ferrite, more Fe$_3$C is exposed leading to galvanic effect and large cathodic site for hydrogen evolution reaction (HER) [24, 28]. The more the cathodic sites which signifies higher pearlite-ferrite ratio, the more the corrosion attack [29, 30]. With increase in applied potential, there was an increase in selective dissolution of ferrite leaving more protruding Fe$_3$C which in turn resulted in increased electrode/electrolyte interface area with the corresponding increase in corrosion rate[9]. It has been reported that increase in carbon content increases the pearlite phase. [4, 31]. It is then expected that the specimens with higher carbon content should possess more pearlite phase which translates to greater cathode to anode ratio with the attendant higher corrosion rate. Fiji ImageJ analysis of the specimens reported previously [32] showed that API 5L X65 steels has larger grain size than steel P110X. Seikh, et al [25], observed higher corrosion rate on steels with small grain microstructures signifying greater surface area for corrosion thereby demonstrating higher susceptibility to corrosion attack. It can therefore

10

be concluded that lower cathode-anode ratio and bigger grain size attributed to steel API 5L X65 presenting less general corrosion rate than steel P110X.

3.3   Surface Analysis of Corrosion Product Formed

Fig. 6 shows SEM micrograph of the steels illustrating the evolution of surface morphology after 24 hours potentiostatic polarization at 100, 150 and 200 $mV_{(OCP)}$ in 3.5 wt% NaCl solution containing CO_2 at 60^0C and pH 6.5.
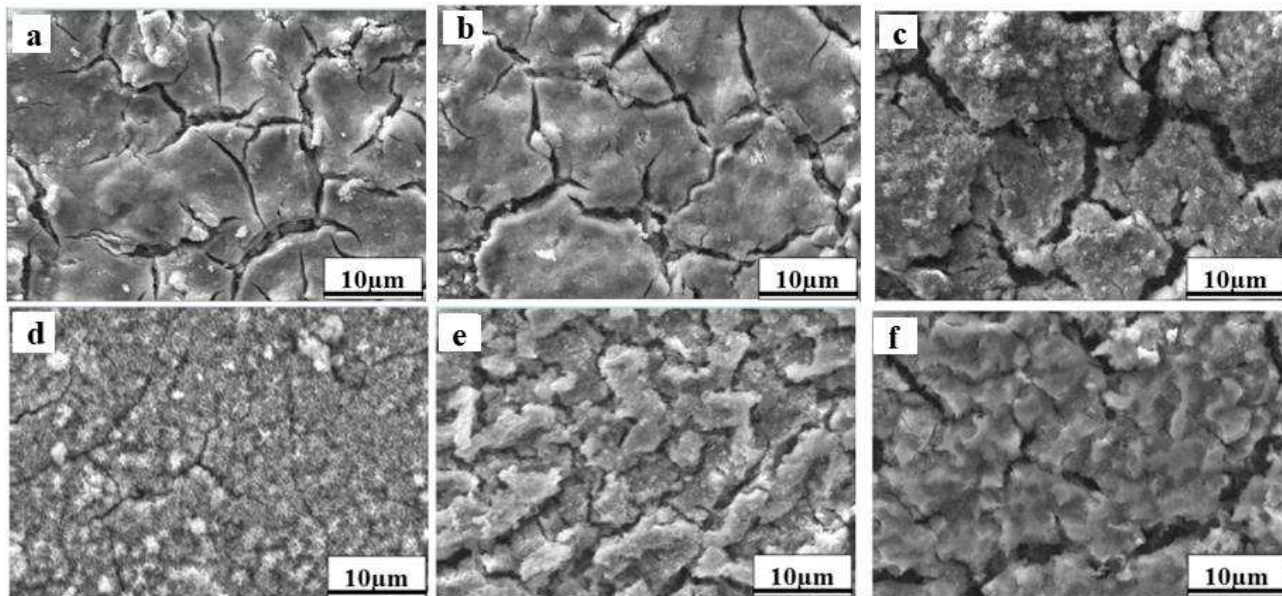

Fig. 6: SEM surface morphology of the specimens after 24 hours potentiostatic polarization in 3.5 wt% NaCl solution containing CO_2 at 60^0C and pH 6.5 for P110X (a) 100 $mV_{(OCP)}$, (b) 150 $mV_{(OCP)}$ and (c) 200$mV_{(OCP)}$; for X65 (d) 100 $mV_{(OCP)}$, (e) 150 $mV_{(OCP)}$ and (f) 200 $mV_{(OCP)}$

The micrographs showed the deposition of porous corrosion layers on the surface of the steels which progressively increased in thickness but decreased in density as the applied potentials increased. This was also revealed by the Fiji ImageJ analysis of the film which showed an increase in percent porosity with increase in applied potentials. The micrographs also showed propagation of cracks on the corrosion layers. These cracks became wider and the corrosion layer less adhesive (flaky) with increase in applied potential indicating the formation of double corrosion layers as presented in Fig. 7 for steel P110X. Similar double corrosion layer has been reported in literature [16, 20, 33] as primary (inner) and secondary (outer) layers respectively. The primary scale was formed directly on the surface of the steel and is usually thin, non-uniform and adherent to the steel surface. On the other hand, the secondary layer is thick, porous and less adherent to the primary layer.
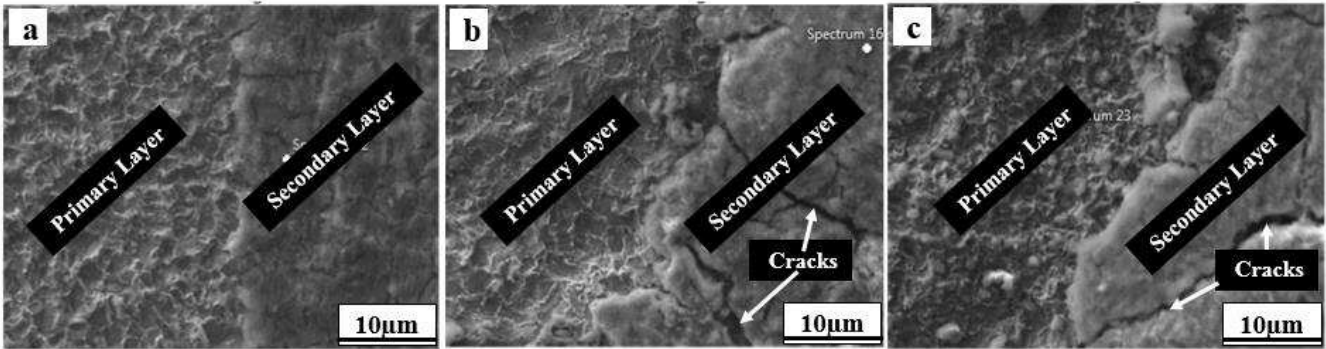
Fig 7: SEM micrographs showing the primary layer and the partially detached secondary layer of steel P110X after 24 hours potentiostatic polarization in 3.5 wt% NaCl solution containing CO_2 at 60^0C and pH 6.5: (a) 100 mV $_{(OCP)}$, (b) 150 mV$_{(OCP)}$ and (c) 200mV$_{(OCP)}$

The increase in thickness of the corrosion layer with increase in the polarization potential is illustrated in the SEM micrographs of the cross-section of the corroded steels shown in Fig. 8 for steel P110X. It can be seen from this figure that the layers are thick and porous with some cracks. Also there are separations between the steels and the scale demonstrating a small gap where electrochemical active species can penetrate and have contact with the steels. This gap is more pronounced at higher scale formation potentials and the contact of the solution under the scale with the steel surface enabled continuous corrosion regardless that the scale appeared to have covered the surface of the steels. This is consistent with the observation of de Moraes, et al [33] indicating the porosity of the corrosion layer. This also could have contributed to the observed high impedance values at higher potentials fitted results of EIS data presented in Table 2
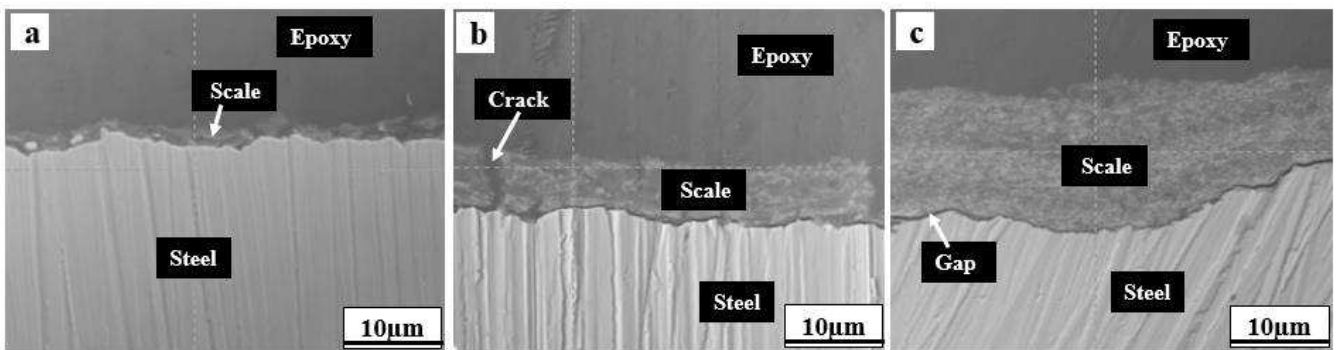

Fig. 8SEM cross section of corrosion products on anodically polarized P110X in 3.5 wt% NaCl solution containing CO_2 at 60^0C and pH 6.5: (a) 100 mV $_{(OCP)}$, (b) 150 mV$_{(OCP)}$ and (c) 200mV$_{(OCP)}$

EDS examination showed that the main elemental composition of the corrosion products are Fe, C, and O with few traces of some alloying elements. The analysis of the corrosion double layer revealed that the primary layer consists of about (average taken from 4 different points on each layer of steel P110X passivated at 150 mV) 87 %Fe, 2 %O_2 and 6 %C while the secondary layer showed about 69 %Fe, 13 %O_2 and 7 %C. This showed that there are more Fe in the primary layer and more O_2 in the secondary

12

layer. The presence of higher oxygen content in the secondary layer is in agreement with the oxide of iron identified by XRD analysis as Fe₃O₄ while the primary layer was identified to consist of mainly Fe₃C. Similar observation was reported by Moiseeva and Rashevskaya [34] ascribing the presence of Fe_3O_4 in the XRD patterns to the decomposition of $Fe(OH)_2$ by the reaction shown in Eq.11.

$$3Fe(OH)_2 \rightarrow Fe_3O_4 + 2H_2O + H_2 \tag{11}$$

Where $Fe(OH)_2$ is the product of the overall anodic electrochemical reaction for ferrous metals as expressed in Eq. 12. This is in accordance with the pH dependent anodic reaction steps proposed by Bockris [35]

$$Fe + 2H_2O \rightarrow Fe(OH)_{2(s)} + 2H^+ + 2e^- \tag{12}$$
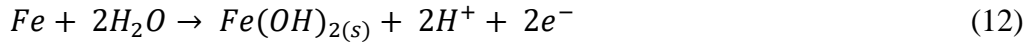
It is interesting to note that the Fe₃C identified in the XRD results is not a corrosion product but merely existed in the scale as a result of its presence in the ferrite-pearlite microstructures as cathode and the ferrite as anode [24, 25, 36].

To assess the extent of pitting, the corrosion products formed on the three repeated test specimens of same composition were cleaned before conducting scan and profilometry tests. Pits were recorded beneath the corrosion products due to the porosity, non-compact and non-adherent characteristics of the corrosion scales. The average depth of ten deepest pits for three repeated specimens were found to be nearly same. Therefore, the deepest among the three test results was utilised for the analysis presented in this work. The SEM micrographs showing the evolution of pits after 24 hours anodic polarization at 100 mV $_{(OCP)}$, 150 mV$_{(OCP)}$ and 200 mV$_{(OCP)}$ in 3.5 wt% NaCl solution containing CO₂ at 60⁰C and pH 6.5 for the two specimens are shown in Fig 9. It is evident from this figure that pits became wider and deeper with increase in applied potentials in agreement with the potentiostatic polarization (increase in current density with increase in anodic potential) and EIS (decrease in capacitive semi-Loop with increase in anodic potential) results of this work. A closer observation of Fig. 9 showed that steel P110X recorded wider but shallow pits than X65 which exhibited deeper but narrow pits.
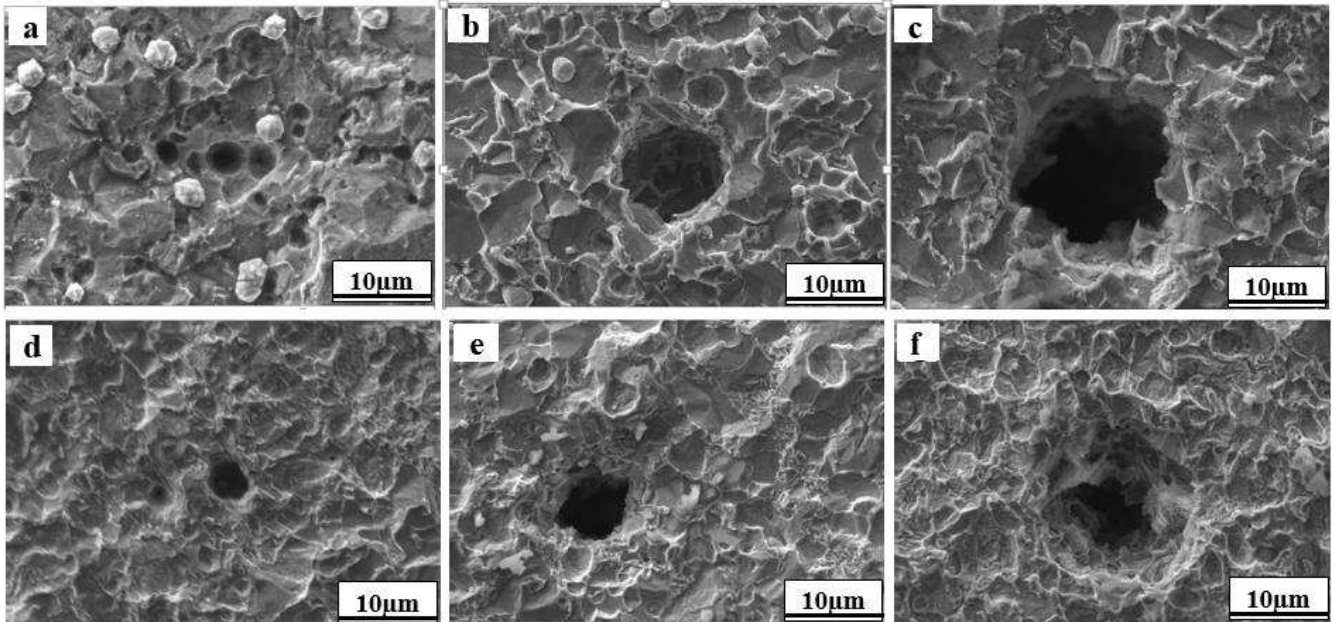
Fig. 9: SEM micrographs of the evolution of pits after 24 hours potentiostatic polarization in 3.5 wt% NaCl solution containing CO_2 at 60^0C and pH 6.5 for P110X (a) 100 mV$_{(OCP)}$, (b) 150 mV$_{(OCP)}$ and (c) 200mV$_{(OCP)}$; for X65 (d) 100 mV$_{(OCP)}$, (e) 150 mV$_{(OCP)}$ and (f) 200 mV$_{(OCP)}$

The identified pits were characterized using multiple region analysis tool of the white light profilometer. The 3D white light profilometry images showing samples of pits with top-ten average (for deepest pits) pits after 24 hours of 100mV$_{(OCP)}$, 150 mV$_{(OCP)}$ and 200 mV$_{(OCP)}$ potentiostatic polarizations in 3.5 wt% NaCl solution containing CO_2 at 60^0C and pH 6.5 are shown in Fig. 10 for steels P110X and X65. These figure demonstrated an increase in pit depth of 22 µm, 40 µm and 73 µm with increase in anodic polarization potentials of 100 mV $_{(OCP)}$, 150 mV $_{(OCP)}$ and 200 mV $_{(OCP)}$ respectively for steel P110X. Also, the same behavioural trend was observed for API 5LX65 steel which recorded pit depths of 45 µm, 69µm and 81µm for 100 mV $_{(OCP)}$, 150 mV $_{(OCP)}$ and 200 mV $_{(OCP)}$ potentials respectively. Similar trend was reported recently for API 5L X65 steel by Mohammed , et al [22].
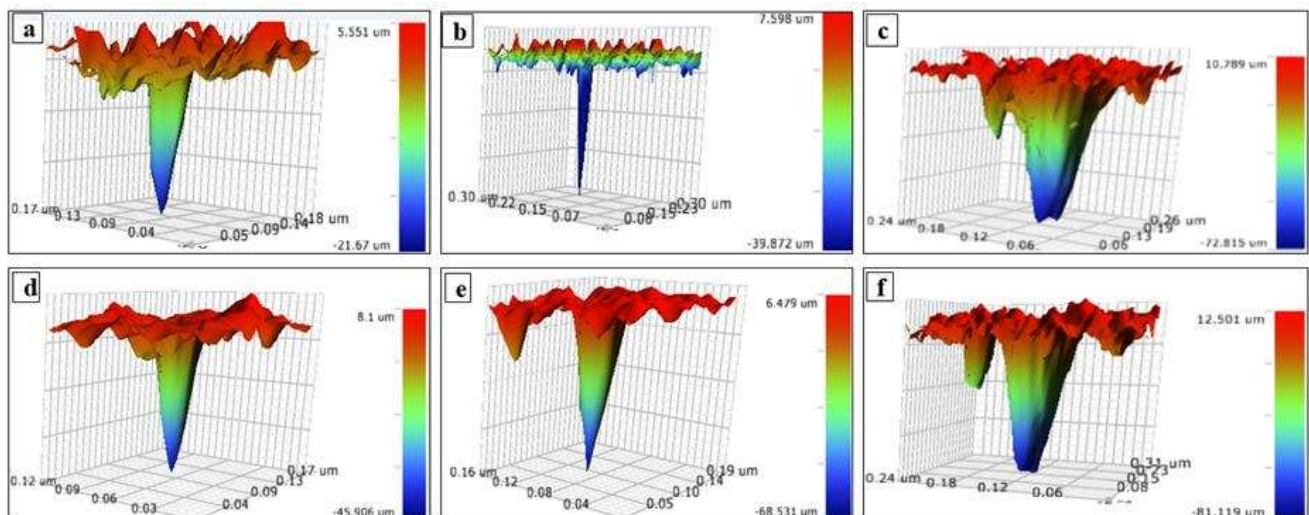

14

Fig 10: 3D White light profilometry images of deepest pit formed on the specimens after 24 h potentiostaic polarization in 3.5 wt% NaCl solution containing CO_2 at 60^0C and pH 6.5 for P110X (a) 100 mV$_{(OCP)}$, (b) 150 mV$_{(OCP)}$ and (c) 200mV$_{(OCP)}$; for X65 (d) 100 mV$_{(OCP)}$, (e) 150 mV$_{(OCP)}$ and (f) 200 mV$_{(OCP)}$

The average maximum pit depth (average of the pit depths recorded at different potentials) for P110X and X65 are 45 µm and 65 µm which corresponds to an average pit penetration rate (pit depth/time) of 16.41 mm/year and 23.75 mm/year respectively. This shows that steel P110X is more resistance to pitting corrosion than API 5L X65 steel which is in agreement with the SEM micrographs of the evolution of pits shown in Fig. 9.

Conclusions

Corrosion products were formed on steels P110X and X65 using anodic polarization potentials of 100 mV$_{(OCP)}$, 150mV$_{(OCP)}$ and 200 mV$_{(OCP)}$ for 24 hours in CO_2 containing 3.5 wt% NaCl solution at 60^0C and pH 6.5. Electrochemical impedance spectroscopy (EIS) and surface analysis methods were used to assess the physical characteristics of the corrosion product films. The results showed that both steels exhibited increase in current density with increase in applied potential. This demonstrated the characteristics behaviour of actively corroding steel which show continues increase in anodic current density with potential within the active region due to activation control reactions. Increase in anodic current density means increased dissolution of iron which corresponds to increase in corrosion rate. This was corroborated with the results of the EIS Nyquist plots which indicated larger capacitive Loops for lower applied potentials.

The properties of the corrosion scales are associated with the chemical composition and microstructure of the steels. Both specimens have ferrite-pearlite microstructures. The specimen with more carbon content obviously showed greater pearlite/ferrite ratio. Pearlite (α-Fe + Fe_3C) is known to act as cathode while ferrite acts as anode. The more the cathodic sites (higher pearlite-ferrite ratio) the more the corrosion attack. Therefore with increase in applied potential, there is an increase in selective dissolution of ferrite leaving more protruding Fe_3C which in turn resulted in increased electrode/electrolyte interface area with the corresponding increase in corrosion rate. This must have contributed to API 5L X65 steel having better general corrosion resistance than Steel P110X. The fine grain size is known to provide large surface area for corrosion attack. This also could have caused the witnessed high uniform corrosion exhibited by steel P110X.

The SEM examination also showed that the corrosion product films formed at higher formation potentials were more porous and non-compact with some cracks on the surface of the corrosion films. These cracks allowed the electrochemical corrosive species to percolate between the steel and corrosion film and there by continued the corrosion attack. The white light profilometry characterization featured maximum pit depths which increased with increase in anodic polarization potentials presenting an average pit penetration rate of 16.41 mm/year and 23.75 mm/year for steels P110X and API 5L X65 respectively. It can therefore be concluded that within the experimental conditions of this work API 5L X65 carbon steel is more prone to pitting corrosion but demonstrated better uniform corrosion resistance than steel P110X.

Acknowledgement

Reference

[1]   T. Baker, "Microalloyed steels, Ironmaking & Steelmaking," ISSN: 0301-9233 (Print) 1743-2812 (Online) Journal homepage, vol. 43, no. 4, pp. 264 - 307, 2016.

[2]   M. Korchynsky, "A New Role for Microalloyed Steels − Adding Economic Value." pp. 26-35.

[3]   S. HSLA, "High-Strength Low-Alloy Steels," in ASM International: Alloying: Understanding the Basics, 2001.

[4]   D. V. Edmonds, and R. C. Cochrane, "The effect of alloying on the resistance of carbon steel for oilfield applications to CO2 corrosion," Materials Research, vol. 8, no. 4, pp. 377-385, 2005.

[5]   W. Morrison, "Overview of microalloying in steel." pp. 25-35.

[6]   Hany Mohamed Abd El-Lateef, Vagif Maharram Abbasov, Leylufer Imran Aliyeva et al., "Corrosion Protection of Steel Pipelines Against CO2 Corrosion - A review," Chemistry Journal, vol. 02, no. 02, pp. 52 - 63, 2012.

[7]   M. Ilman, "Analysis of internal corrosion in subsea oil pipeline," Case Studies in Engineering Failure Analysis, vol. 2, no. 1, pp. 1-8, 2014.

[8]   A. Dugstad, H. Hemmer, and M. Seiersten, "Effect of steel microstructure on corrosion rate and protective iron carbonate film formation," Corrosion, vol. 57, no. 4, pp. 369-378, 2001.

[9]   J. Sun, G. Zhang, W. Liu et al., "The formation mechanism of corrosion scale and electrochemical characteristic of low alloy steel in carbon dioxide-saturated solution," Corrosion Science, vol. 57, pp. 131-138, 2012.

[10]   Y. Zhang, X. Pang, S. Qu et al., "Discussion of the CO_2 corrosion mechanism between low partial pressure and supercritical condition," Corrosion Science, vol. 59, pp. 186-197, 2012.

[11] G. Schmitt, and M. Horstemeier, "Fundamental aspects of CO2 metal loss corrosion-Part II: Influence of different parameters on CO2 corrosion mechanisms."

[12] R. Vera, F. Vinciguerra, and M. Bagnara, "Comparative Study of the Behavior of API 5L-X65 Grade Steel and ASTM A53-B Grade Steel against Corrosion in Seawater," Int. J. Electrochem. Sci, vol. 10, pp. 6187-6198, 2015.

[13] H. Luo, C. Dong, K. Xiao et al., "Passive Film Properties and Electrochemical Behavior of Co-Cr-Mo Stainless Steel in Chloride Solution," Journal of Materials Engineering and Performance, vol. 26, no. 5, pp. 2237-2243, 2017.

[14] C. Della Rovere, J. Alano, J. Otubo et al., "Corrosion behavior of shape memory stainless steel in acid media," Journal of Alloys and Compounds, vol. 509, no. 17, pp. 5376-5380, 2011.

[15] C. Della Rovere, J. Alano, R. Silva et al., "Characterization of passive films on shape memory stainless steels," Corrosion Science, vol. 57, pp. 154-161, 2012.

[16] C. Palacios, and J. Shadley, "Characteristics of corrosion scales on steels in a CO2-saturated NaCl brine," Corrosion, vol. 47, no. 2, pp. 122-127, 1991.

[17] M. Kermani, and A. Morshed, "Carbon dioxide corrosion in oil and gas production-A compendium," Corrosion, vol. 59, no. 8, pp. 659-683, 2003.

[18] M. Alizadeh, and S. Bordbar, "The influence of microstructure on the protective properties of the corrosion product layer generated on the welded API X70 steel in chloride solution," Corrosion Science, vol. 70, pp. 170-179, 2013.

[19] G.-X. Zhao, X.-H. Lu, J.-M. Xiang et al., "Formation characteristic of CO 2 corrosion product layer of P110 steel investigated by SEM and electrochemical techniques," Journal of Iron and Steel Research, International, vol. 16, no. 4, pp. 89-94, 2009.

[20] M. A. Islam, and Z. N. Farhat, "Characterization of the Corrosion Layer on Pipeline Steel in Sweet Environment," Journal of Materials Engineering and Performance, vol. 24, no. 8, pp. 3142-3158, 2015.

[21] A. G. 94, "Standard Guide for Examination and Evaluation of Pitting Corrosion," Designation: G 46 – 94 (Reapproved 2005), ASTM International,, 2005.

[22] S. Mohammed, Y. Hua, R. Barker et al., "Investigating pitting in X65 carbon steel using potentiostatic polarisation," Applied Surface Science, vol. 423, pp. 25-32, 2017.

[23] C. Yu, X. Gao, and P. Wang, "Electrochemical Corrosion Performance of Low Alloy Steel in Acid Sodium Chloride Solution," Electrochemistry, vol. 83, no. 6, pp. 406-412, 2015.

[24] S. Al-Hassan, B. Mishra, D. Olson et al., "Effect of microstructure on corrosion of steels in aqueous solutions containing carbon dioxide," Corrosion, vol. 54, no. 6, pp. 480-491, 1998.

[25] A. H. Seikh, "Influence of Heat Treatment on the Corrosion of Microalloyed Steel in Sodium Chloride Solution," Journal of Chemistry, vol. 2013, 2013.

[26] H. Luo, C. Dong, X. Li et al., "The electrochemical behaviour of 2205 duplex stainless steel in alkaline solutions with different pH in the presence of chloride," Electrochimica Acta, vol. 64, pp. 211-220, 2012.

[27] H. Luo, S. Gao, C. Dong et al., "Characterization of electrochemical and passive behaviour of Alloy 59 in acid solution," Electrochimica Acta, vol. 135, pp. 412-419, 2014.

[28] D. Lopez, T. Perez, and S. Simison, "The influence of microstructure and chemical composition of carbon and low alloy steels in CO 2 corrosion. A state-of-the-art appraisal," Materials & Design, vol. 24, no. 8, pp. 561-575, 2003.

[29] L. T. Popoola, A. S. Grema, G. K. Latinwo et al., "Corrosion problems during oil and gas production and its mitigation," International Journal of Industrial Chemistry, vol. 4, no. 1, pp. 1-15, 2013.

[30] P. Sarkar, P. Kumar, M. K. Manna et al., "Microstructural influence on the electrochemical corrosion behaviour of dual-phase steels in 3.5% NaCl solution," Materials Letters, vol. 59, no. 19, pp. 2488-2491, 2005.

[31] J. Guo, S. Yang, C. Shang et al., "Influence of carbon content and microstructure on corrosion behaviour of low alloy steels in a Cl− containing environment," Corrosion Science, vol. 51, no. 2, pp. 242-251, 2009.

[32] L. Onyeji, G. M. Kale, and B. M. Kermani, "Comparative Studies of the Effects of Microstructures on the Corrosion Behavior of Micro Alloyed Steels in Unbuffered 3.5 Wt% NaCl Saturated With CO_2," World Academy of Science, Engineering and Technology, International Journal of Chemical, Molecular, Nuclear, Materials and Metallurgical Engineering, vol. 11, no. 2, pp. 131-138, 2017.

[33] F. de Moraes, J. R. Shadley, J. Chen et al., "Characterization of CO2 corrosion product scales related to environmental conditions."

[34] L. Moiseeva, and N. Rashevskaya, "Effect of pH value on corrosion behavior of steel in CO 2-containing aqueous media," Russian journal of applied chemistry, vol. 75, no. 10, pp. 1625-1633, 2002.

[35] J. M. Bockris, D. Drazic, and A. Despic, "The electrode kinetics of the deposition and dissolution of iron," Electrochimica Acta, vol. 4, no. 2, pp. 325-361, 1961.

[36] S. Nešić, "Key issues related to modelling of internal corrosion of oil and gas pipelines–A review," Corrosion Science, vol. 49, no. 12, pp. 4308-4338, 2007.